Large Mesoscale Convection and Sea Breeze Circulation. Part I: Linear Stability Analysis

WEN-YIH SUN

Department of Geosciences, Purdue University, West Lafayette, IN 47907

ISIDORO ORLANSKI

Geophysical Fluid Dynamics Laboratory/NOAA, Princeton University, Princeton, NJ 08540

(Manuscript received 12 November 1980, in final form 20 April 1981)

ABSTRACT

The interactions between the sea breeze circulation and trapeze instability are investigated using a set of linearized equations. The results show that mesoscale waves associated with trapeze instability can be easily triggered by the sea breeze circulation and can propagate far inland, but no mesoscale waves are observed over the ocean. The wavelength is a few hundred kilometers. The period of the waves, which depends on the Coriolis parameter, eddy viscosity and the strength of land-sea contrast, can be either one day or two days, or a combination of one and two days. The waves obtained here are similar to the cloud bands observed in West Africa and South America.

1. Introduction

The diurnal variation of wind, temperature and pressure in the lower troposphere has been studied by many scientists. Blackadar (1957) and Buajitti and Blackadar (1957) proposed that the diurnal variation of the wind comes from the changes in frictional drag associated with the diurnal variation in the stratification of the planetary boundary layer (PBL). At a fixed level in the boundary layer these mechanisms give rise to an elliptical or circular wind hodograph rotating clockwise with time. Blackadar (1957) reproduced a pronounced jet, with peak speed occurring near 0600 LST, in a model of the winter northeast trades at Fort Larmy, Chad (12°N). Ing (1971) successfully applied this mechanism to explain the nocturnal rainfall maximum over the Korat Plateau, Thailand, during the summer monsoon. But McGarry and Reed (1978), in their study of diurnal variation in convective activity in West Africa and the GATE region, found that Blackadar's theory failed to explain the observed patterns over the northern part of the land (~15–20°N). Thunderstorm activity was most intense in the late afternoon or early evening, and rainfall amounts were greatest shortly before midnight. The data over West Africa show little evidence of any substantial, clockwise-rotating departure vector as observed in the Korat Plateau. There is evidence of a sizeable linear fluctuation in wind speed, suggesting that the largest convergence and vorticity occurs in the afternoon. McGarry and Reed's data show that the maximum rainfall over large areas is quite uniform in time. They give little or no evidence of significant longitudinal differences in the time of occurrence of the maximum, as would be required if afternoon showers in certain regions propagate downstream and produce nocturnal maxima in other regions as suggested by Cocheme and Franquin (1967). McGarry and Reed also concluded that the radiative mechanism is unlikely to be responsible for the enhanced nocturnal rainfall in this area. Therefore, they proposed that the small, isolated convective elements with vigorous growth in the late afternoon later merge to form the squall lines or organized clusters over West Africa. These clusters or squall systems represent a new level of convective organization which, as noted by Cocheme and Franquin and confirmed by Martin's (1975) statistics, has a longer lifetime than isolated convective clouds. If these long-lived systems tend to reach their peak intensity about 6 h after the time of formation, the 2200 LST rainfall maximum is accounted for satisfactorily.

Well-organized squall lines or cloud clusters also are observed in tropical South America. Fig. 1 is a satellite picture in which cloud bands are aligned parallel to the coast from the equator to 15°S. The distance between cloud bands is a few hundred kilometers. Clear skies are noted to the west and east of these bands in both the eastern Pacific and western Atlantic Ocean. The cloud elements are

0022-4928/81/081675-19$08.75

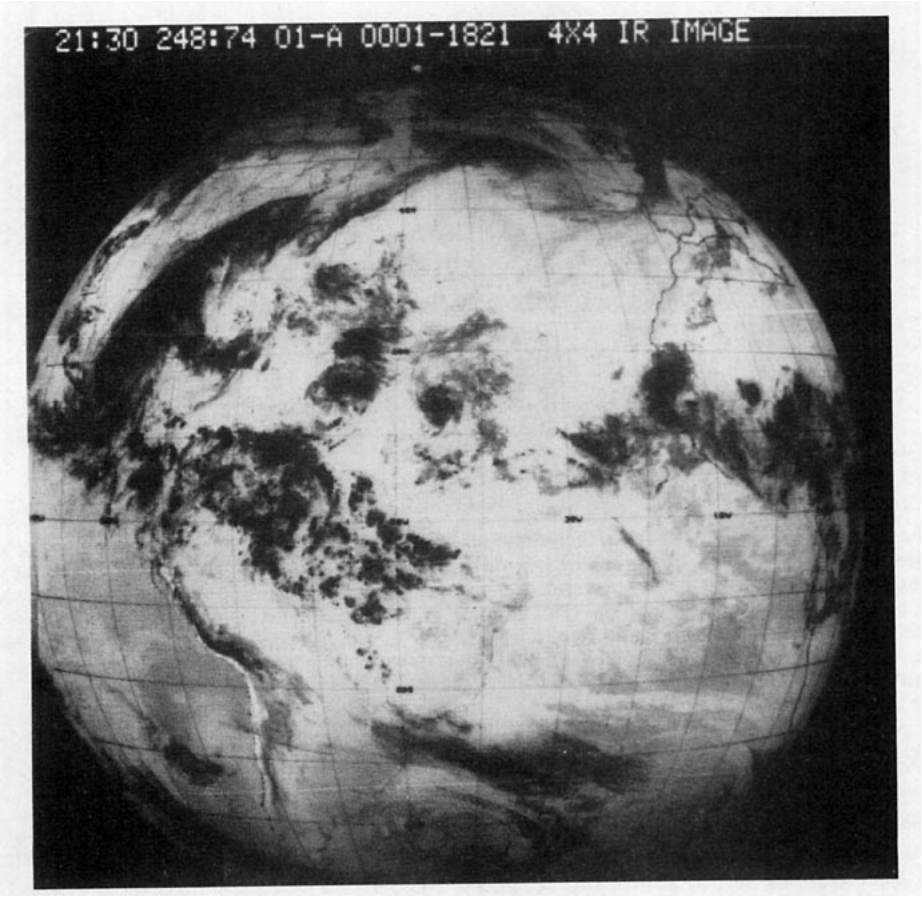

FIG. 1. GOES East satellite picture at 2130 GMT 5 September 1974, showing three cloud bands aligned parallel to the coast of South America. Their horizontal wavelength is of a few hundred kilometers. There is a clear sky off the coast.

organized into lines parallel to the coast and extend several hundred kilometers inland. Such cloud bands are quite often observed in the late afternoon or evening, but the location of the cloud bands can be different from one day to another. Kousky (1980) has studied the diurnal rainfall variation in northeastern Brazil using the rainfall data for the period 1961–70. He has concluded that the precipitation in most coastal areas is due to the sea breeze circulation, and in the interior area is due to the mountain-valley breeze. However, the contours of rainfall appear to lie parallel to the coastline instead of the contours of elevation, and the locations vary from day to day. Both suggest more study is required before this phenomenon is understood. The mesoscale cloud bands are also observed in northwestern South America. The location of these bands is also different from one day to another.

Orlanski (1976b) observed the cloud bands with a horizontal wavelength of 500 km and a two-day period in West Africa during the nighttime. Also, Orlanski's (1973) study points out that the diurnal variability of the atmospheric boundary layer could be one of the major sources of internal gravity waves. One of his results was that the diurnal variation of the atmospheric static stability has a destabilizing effect on the atmospheric boundary layer, and the available potential energy is released in the form of gravity waves that range from a period of two days down to a few hours, with horizontal scales of a few hundred kilometers to 1 km. His results, from an inviscid fluid model, show that the growth rate of the unstable low-frequency waves are highly dependent on latitude, mainly because inertial-internal gravity waves cannot have periods larger than the local inertial period. For instance, the 2-day wave could only extend from 15°N to 15°S and the 1-day wave from 30°N to 30°S. He also found that the most unstable waves due to trapeze instability in the equatorial region ($f = 0$) have 2-day periods and ~400 km wavelengths. Orlanski (1976b) extended the linear results with the use of a two-dimensional nonlinear numerical model. This new study of trapeze instability in an equatorial β-plane included a more realistic wind profile and the effect of moisture.

The mechanism proposed by Orlanski may explain how the cloud elements can develop into organized cloud lines. But the growth rate of the trapeze instability is very small, it may take quite

a few days for random clouds to become organized into a mesoscale wave without any other energy supply. A strong contrast between land and ocean, cloud distributions and the special orientation of cloud lines like those in Fig. 1 cannot be explained by Orlanski's model because his environmental condition is horizontally uniform. It is also puzzling that the organized clouds in equatorial South America have a 1-day period instead of the 2-day period suggested by Orlanski. In their spectral analysis of cloudiness over Africa, Orlanski and Polinsky (1977) showed (see Fig. 2) that the contribution to the cloudiness from waves of short period (i.e., period less than or equal to 3 days) is more important than that from the waves of long period (i.e., period longer than 3 days). However, at the same time, the 1-day wave is slightly more important than the 2-day wave. It also is noted from satellite pictures, as shown by Orlanski (1976), that 2-day waves more clearly show up during the night, but 1-day waves more clearly show up during the daytime.

It seems important to investigate the differences that may arise due to trapeze instability as proposed by Orlanski, where more realistic conditions such as the local atmospheric variability in the stratification, land-sea contrast, and the variation of the eddy viscosity are considered in an attempt to explain the regional differences among unstable waves. In particular, persistent 1-day oscillations in organized cloud patterns are observed in equatorial South America. Also, Orlanski and Polinsky found mixed 1- and 2-day waves over Africa, instead of the slightly more unstable 2-day waves predicted by Orlanski's simple model. Therefore, this paper will investigate the effects of land-sea contrast, viscosity and the diurnal variation of stratification in the planetary boundary layer on the trapeze instability. The results will show that mesoscale internal gravity waves associated with local trapeze instability can be excited by the sea breeze circulation near the coast, where the cloud bands originate, and then develop and spread inland. Organized cloud bands, however, cannot develop over the ocean. The amplitude of variables obtained are associated with the strength of the sea breeze circulation and other factors, because a nonhomogeneous equation is used here. The period of mesoscale waves in the equatorial region depends on the diurnal variation of stratification as well as on the magnitude of the viscosity. The general features of the results of both the linear analysis and the nonlinear numerical models are very encouraging when compared with observations.

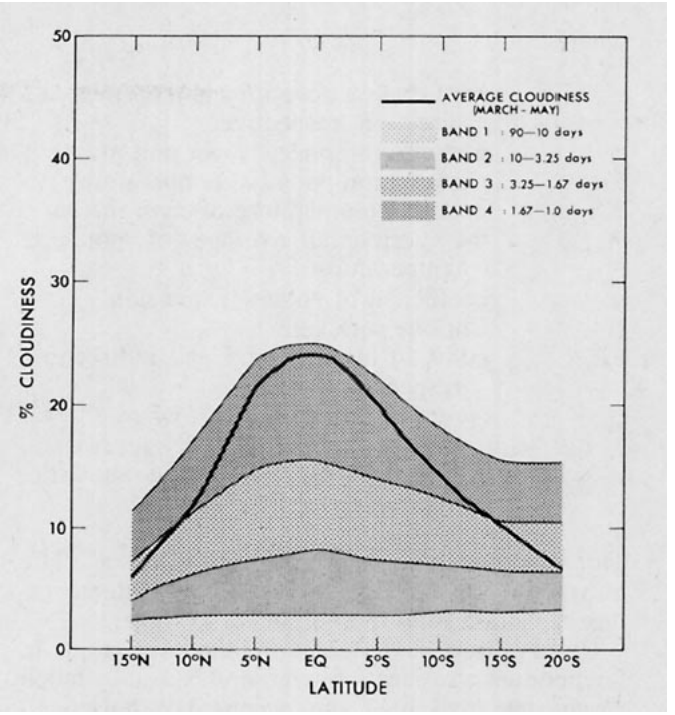

FIG. 2. A comparison between the average cloudiness for the 3-month period (March–May 1975) and the square root of each band-averaged contribution of variance (after Orlanski and Polinsky, 1977).

2. The linear model

a. Formulation of equations

The circulation studied here is produced by the diurnal variation of stratification near the ground surface and the strong temperature contrast between land and ocean. The vertical scale of motion is considerably smaller than the scale height, $H_s = RT/g$, and the velocities involved here are much smaller than the velocity of sound. Therefore, the Boussinesq approximation is valid. The two-dimensional, linearized equations for an initially motionless fluid and Prandtl number of unity are

$$\frac{\partial u'}{\partial t} - fv' = -\frac{\partial p'}{\partial x} + \nu_x \frac{\partial^2 u'}{\partial x^2} + \nu_z \frac{\partial^2 u'}{\partial z^2}, \quad (2.1)$$

$$\frac{\partial v'}{\partial t} + fu' = \nu_x \frac{\partial^2 v'}{\partial x^2} + \nu_z \frac{\partial^2 v'}{\partial z^2}, \quad (2.2)$$

$$C_1 \frac{\partial w'}{\partial t} = -\frac{\partial p'}{\partial z} + g\alpha(\tilde{\theta} + \theta' - \bar{\theta}) + C_1\left(\nu_x \frac{\partial^2 w'}{\partial x^2} + \nu_z \frac{\partial^2 w'}{\partial z^2}\right), \quad (2.3)$$

$$\frac{\partial \theta'}{\partial t} + u' \frac{\partial \tilde{\theta}}{\partial x} + w' \frac{\partial \tilde{\theta}}{\partial z} = \nu_x \frac{\partial^2 \theta'}{\partial x^2} + \nu_z \frac{\partial^2 \theta'}{\partial z^2}, \quad (2.4)^1$$

$$\frac{\partial u'}{\partial x} + \frac{\partial w'}{\partial z} = 0, \quad (2.5)$$

[1] The assumption $\nu\nabla^2\tilde{\theta} \ll \partial\tilde{\theta}/\partial t$ has been used to obtain this equation.

where

u', v', w'	perturbation velocities in the x, y and z direction, respectively
p'	perturbation pressure per unit mass
θ'	perturbation potential temperature
$\tilde{\theta}(x, z, t)$	potential temperature of environment
$\bar{\theta}(z, t)$	the horizontal average of potential temperature
α	coefficient of volume expansion
f	Coriolis parameter
ν_x, ν_z	eddy diffusivities in x and z direction, respectively
C_1	a controllable parameter, where $C_1 = 1$ for the non-hydrostatic approximation, and $C_1 = 0$ for the anelastic, hydrostatic approximation.

The total potential temperature $\theta = \tilde{\theta} + \theta'$. The buoyancy term in (2.3) just comes from the temperature deviation from the horizontal average.

Observations show that horizontal variations in temperature stratification over land is usually much larger than that over the ocean. The horizontal average of potential temperature $\bar{\theta}$ does not well represent the temperature either over land or over the ocean. Therefore, $\tilde{\theta}(x, z, t)$ is introduced into the thermodynamic equation in (2.4), so that the difference of the stratification between land and ocean can be taken into consideration.

Eqs. (2.1)–(2.5) can be combined into the single equation

$$\left(\frac{\partial}{\partial t} - \nu\nabla^2\right)^2\left(\frac{\partial^2 w'}{\partial z^2} + C_1\frac{\partial^2 w'}{\partial x^2}\right) + f^2\frac{\partial^2 w}{\partial z^2} = g\alpha\frac{\partial^2}{\partial x^2}\left(-w'\frac{\partial\tilde{\theta}}{\partial z} - u'\frac{\partial\tilde{\theta}}{\partial x} + \frac{\partial\tilde{\theta}}{\partial t}\right), \quad (2.6)^2$$

where

$$\nu\nabla^2 = \nu_x\frac{\partial^2}{\partial x^2} + \nu_z\frac{\partial^2}{\partial z^2}.$$

Eqs. (2.5) and (2.6) contain two variables u' and w'. If the boundary conditions are well-posed, u' and w' can be solved from (2.5) and (2.6).

Since the horizontal wavelength is much larger than the vertical wavelength in this study, the hydrostatic approximation is justified. Hence, we can set $C_1 = 0$ to avoid solving the Poisson equation at each time step, which is very time consuming. (2.6) can be written as

$$\frac{\partial^2}{\partial z^2}\phi = g\alpha\frac{\partial^2}{\partial x^2}\left(-w'\frac{\partial\tilde{\theta}}{\partial z} - u'\frac{\partial\tilde{\theta}}{\partial x} + \frac{\partial\tilde{\theta}}{\partial t}\right), \quad (2.7)$$

where

$$\phi = \left(\frac{\partial}{\partial t} - \nu\nabla^2\right)^2 w' + f^2 w' = \frac{\partial^2 w'}{\partial t^2} - 2\nu\nabla^2\frac{\partial w'}{\partial t} + \nu^2\nabla^4 w' + f^2 w' - \frac{\partial\nu}{\partial t}\nabla^2 w'. \quad (2.8)$$

Eq. (2.8) can be solved numerically. The primed notation will be dropped hereafter. Eq. (2.8) can be expressed in finite-difference form as

$$\frac{w_{i,j}^{n+1} - 2w_{i,j}^n + w_{i,j}^{n-1}}{\Delta t^2} = \phi_{i,j}^n + 2\nu\nabla^2\left(\frac{w_{i,j}^n - w_{i,j}^{n-1}}{\Delta t}\right) - \nu^2\nabla^4 w_{i,j}^n - f^2 w_{i,j}^n + \frac{\partial\nu}{\partial t}\nabla^2 w_{i,j}^n. \quad (2.9)$$

Now $\phi_{i,j}^n$ can be obtained by solving (2.7), i.e.,

$$\frac{\phi_{i,j+1}^n - 2\phi_{i,j}^n + \phi_{i,j-1}^n}{\Delta z^2} = g\alpha\frac{\partial^2}{\partial x^2}\left(-w^n\frac{\partial\tilde{\theta}}{\partial z} - u^n\frac{\partial\tilde{\theta}}{\partial x} + \frac{\partial\tilde{\theta}^n}{\partial t}\right). \quad (2.10)$$

Eq. (2.10) is a tridiagonal system (i.e., $j+1, j, j-1$) for each i, it can be solved directly, with $\phi_{i,j}^n = 0$ at top and bottom. Subsequently, w^{n+1} can be obtained by (2.9), and u^{n+1} can be obtained by solving the continuity equation, giving

$$\frac{u_{i+1,j}^{n+1} - u_{i,j}^{n+1}}{\Delta x} = 0.5\left[\left(\frac{\partial w}{\partial z}\right)_{i+1,j}^{n+1} + \left(\frac{\partial w}{\partial z}\right)_{i,j}^{n+1}\right]. \quad (2.11)$$

The potential temperature of the basic state is given by

$$\tilde{\theta}(x, z, t) = \tilde{\theta}(z_T) - \int_z^{z_T}\frac{N_0^2}{g\alpha}dz - \frac{0.5C_2}{g\alpha} \times \cos[\omega(t - t_0)]\{A - \tanh[B(x - x_0)]\} \times \int_z^{zT}\{1.0 - \tanh[C_3(z' - z_0)]\}dz', \quad (2.12)$$

where $\tilde{\theta}(z_T)$ is $\tilde{\theta}(x, z, t)$ at the upper boundary z_T (= 10 km); $N_0^2 = 1.0 \times 10^{-4}$ s^{-2}; x_0 is the location of the coast; z_0 is the height of the mixing layer; A, B and C_3 are parameters; $C_2 = N_0^2/(A + 1)$, ω is angular velocity of the earth rotation; and $t_0 = 2$ h. The parameters A and B control the strength of the land-sea contrast, and parameter C_3 determine the depth of the boundary layer. From (2.12) we can calculate the Brunt-Väisälä frequency as

$$N^2(x, z, t) = g\alpha\frac{\partial\tilde{\theta}(x, z, t)}{\partial z} = N_0^2 + 0.5C_2\{A - \tanh[B(x - x_0)]\} \times \{1.0 - \tanh[C_3(z - z_0)]\} \times \cos[\omega(t - t_0)]. \quad (2.13)$$

[2] See Appendix B.

The stratification given by (2.13) represents a strong diurnal variation in the mixed layer over the land, but weak to no diurnal variation over the ocean. Notice that the stratification given by (2.13) is similar to that studied by Orlanski (1973), except that a term expressing the horizontal variation due to land-sea contrast has been included. A diurnal variation of viscosity is also included in this study.

Since the forcing function $\tilde{\theta}$ is a function of x, z and t, the perturbation variables u and w interact with $\tilde{\theta}$ in both the x and z directions through (2.10). The normal mode assumption in the x direction cannot satisfy this system. Therefore, these equations cannot be simplified into a one-dimensional problem as done by Orlanski (1973).

Since we are interested in the mesoscale circulation, Shuman's smoothing operator is applied to the vertical velocity along the horizontal direction at each time step, in order to damp short-wavelength noise. Shuman's filter is expressed as

$$\tilde{w}_{i,j} = w_{i,j} + \tfrac{1}{2}S_h(w_{i-1,j} - 2w_{i,j} + w_{i+1-j}). \quad (2.14)$$

S_h is the coefficient of Shuman smoothing, and is assigned a value of 0.25 in this linear stability analysis. The corresponding eddy coefficient from Shuman's smoothing is

$$\nu_s = \frac{1}{2} S_h \frac{\Delta x^2}{\Delta t}. \quad (2.15)$$

The sea breeze circulation has been studied by many investigators with both linearized equations and nonlinear numerical models. In their linearized model, Mak and Walsh (1976) assumed, as have others, that the amplitudes of the variables were constant with time. Therefore, unstable internal gravity waves could not exist in their solution. On the other hand, the real time simulated in most numerical models is limited to one or two days, which is not long enough to allow any weakly unstable waves to grow. Hence, the mesoscale cloud bands near the equator in West Africa and South America with wavelengths of a few hundred kilometers have never been reproduced by any sea breeze circulation model.

b. Domain and boundary conditions

The domain of the model used to study the linearized equations is 1200 km × 10 km, and the land occupies two-thirds and the ocean one-third of total domain. The grid intervals are 12 km in the x direction, and 0.2 km in the z direction.

The vertical velocity w is assumed zero at the top (z = 10 km) and bottom. The open boundary condition proposed by Orlanski (1976a) has been applied to the lateral boundaries for w. The horizontal velocity u is set to zero at x = 1200 km. As mentioned before, the diurnal variation of the stratification is very weak or vanishes over the oceans, and the amplitude of waves produced by trapeze instability over the ocean should be much smaller than that over land. The distance between the coast and the lateral boundary is 400 km, which is much larger than the horizontal scale of most sea breeze models. Hence, the horizontal velocity u is set equal to zero at the lateral boundary over the ocean. This should not significantly affect the solutions inside the domain. The constraint of $u = 0$ on the lateral boundary over the ocean will be dropped in the second part of this paper, where open lateral boundary conditions will be applied in a fully nonlinear numerical model (Sun and Orlanski, 1981).

Before presenting the results, we again look at the equations. In case of no viscosity and no differential thermal forcing across the coastline, Eqs. (2.3) and (2.4) become

$$C_1 \frac{\partial w'}{\partial t} = -\frac{\partial p'}{\partial z} + g\alpha\theta',$$

$$\frac{\partial \theta'}{\partial t} + w' \frac{\partial \bar{\theta}}{\partial z} = 0.$$

Combining these two equations with horizontal momentum equations and continuity equation yields

$$w'_{ttzz} + f^2 w'_{zz} + \nabla_h^2[C_1 w'_{tt} + N^2(z,t)w'] = 0. \quad (2.16)^3$$

where $\nabla_h = \partial^2/\partial x^2 + \partial^2/\partial y^2$. This equation has been discussed in detail by Orlanski (1973) for a nonhydrostatic model (C = 1) and with a stratification given by

$$N^2 = N_0^2 + N_1^2 \cos\omega t. \quad (2.17)$$

If the solution of (2.16) is in the form of $w = W_0 \sin[m\pi(z)/h]e^{i(kx+ly)}$, where h is the height of the atmosphere, (2.16) can be converted into a Mathieu equation

$$W_{0_{tt}} + \left\{ \frac{(k^2 + l^2)N_0^2 + (m\pi/h)^2 f^2}{C_1(k^2 + l^2) + (m\pi/h)^2} + \frac{(k^2 + l^2)N_1^2}{C_1(k^2 + l^2) + (m\pi/h)^2} \cos\omega t \right\} W_0 = 0. \quad (2.18)$$

The general solution of (2.18) is

$$W_0 = G_1 e^{\sigma t}\phi(2t/\omega) + G_2 e^{\sigma t}\phi(-2t/\omega), \quad (2.19)$$

where ϕ is a periodic function of the variable $2t/\omega$ and σ = the growth rate which depends on the parameters N_0^2, N_1^2, k, l, etc. G_1 and G_2 in (2.19) are arbitrary constants.

For the particular case in which $f = 0$, Fig. 3 shows the contours of nondimensional growth rate $\sigma_N = 2\sigma/\omega$ as a function of the nondimensional horizontal scale $(k^2 + l^2)^{1/2}h2N_0/(\omega\pi)$ and the ratio

[3] See Eq. (B12) in Appendix B.

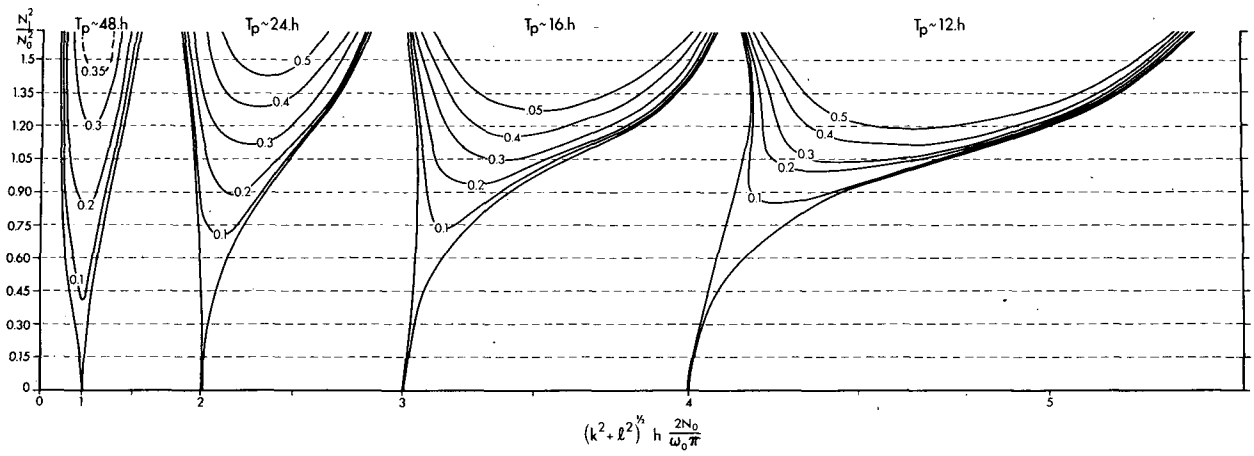

FIG. 3. Contours of nondimensional growth rate $\mu = 2\sigma/\omega$, as a function of the nondimensional horizontal scale and the ratio N_1^2/N_0^2. The predominant oscillatory period in the different branches is indicated as T_p (after Orlanski, 1976).

N_1^2/N_0^2. The different branches correspond to distinct oscillation periods of the function $\phi(2t/\omega)$. The first branch is approximately a 2-day period, the second a 1-day period, and so on. As can be seen, the most unstable waves for $N_1^2/N_0^2 < 1$ correspond to the first branch with a two-day period, and the e-folding time is longer than one day. The horizontal wavelength is ~600 km if h is 2 km.

3. Solution of linearized equations

The complexity of the previous example can be increased by adding to the heat equation the forcing of the sea breeze circulation without horizontal variation of stratification.

a. Case A; $f = 0$

If the horizontal variation of the stratification is ignored, then the heat equation (2.4) becomes

$$\frac{\partial\theta'}{\partial t} + w'\frac{\partial\bar{\theta}'}{\partial z} = \nu_x\frac{\partial^2\theta'}{\partial x^2} + \nu_z\frac{\partial^2\theta'}{\partial z^2}. \quad (3.1)$$

Eq. (3.1) has been used by Mak and Walsh (1976) and others in their sea breeze studies. As mentioned before, $\bar{\theta}$ is not suitable to represent the potential temperature either over the land or over the ocean. Here we just assume $\bar{\theta}$ is equal to the potential temperature over land, because the area of land is twice as large as the ocean area in our case. Another reason is that a strong diurnal variation of $\bar{\theta}$ is required to produce a trapeze instability in this system. If (2.4) is replaced by (3.1), the following equation can be obtained:

$$\left(\frac{\partial}{\partial t} - \nu\nabla^2\right)^2\frac{\partial^2 w'}{\partial z^2} + C_1\frac{\partial^2 w'}{\partial x^2} + f^2\frac{\partial^2 w}{\partial z^2} = g\alpha\frac{\partial^2}{\partial x^2}\left(-w'\frac{\partial\bar{\theta}}{\partial z} + \frac{\partial\bar{\theta}}{\partial t}\right). \quad (3.2)$$

Comparing (3.2) with (2.6), $\partial\bar{\theta}/\partial t$ still remains in (3.2) as a forcing term to produce sea breeze circulation.

The parameters in (2.13) are $N_0^2 = 1.0 \times 10^{-4}$ s^{-2}, $x_0 = 7.8 \times 10^7$ cm, $C_3 = 1.0/(2.5 \times 10^4$ cm), $z_0 = 1.5 \times 10^5$ cm, $A = 1.5$, $B = 1/2 \times 10^6$ cm, $C_2 = 1.0 \times 10^{-4}/\{A - \tanh(-Bx_0)\}$, $t_0 = 2h$, and the eddy viscosity is given by

$$\nu_z = \begin{cases} \nu_0\cos\omega(t - 14\text{ h}), \\ \qquad \text{if} \quad \cos\omega(t - 14\text{ h}) > C_{\min} \\ \nu_0 C_{\min}, \\ \qquad \text{if} \quad \cos\omega(t - 14\text{ h}) \leq C_{\min} \end{cases}. \quad (3.3)$$

Here $\nu_0 = 9.26 \times 10^2$ cm^2 s^{-1}, $C_{\min} = 0.1$, and the eddy viscosity in the x direction is given by

$$\nu_x = 3.6 \times 10^3\nu_z \quad (3.4)$$

for this particular case. The artificial eddy viscosity associated with Shuman's smoothing, ν_s is 3.6×10^5 m^2 s^{-1} in the horizontal direction, which is much larger than ν_x. Notice that ν_z used here is much smaller than that in most sea breeze models, since the variation of the environmental potential temperature profile is given by $\bar{\theta}$ in this model, while it requires a strong vertical viscosity to produce a reasonable stratification profile in most sea breeze models.

In order to avoid solving the Poisson equation, C_1 is assumed to be zero in (2.6) and (2.16) hereafter. The numerical integration starts from 0000 h of day 0. The vertical cross-section of the vertical velocity at 1400 LST of day 1 is presented in Fig. 4a. A sea breeze circulation clearly appears in this diagram, with upward motion on the warm side (i.e., land) of the coast and downward motion on the cold side (i.e., ocean). The amplitude of the upward motion is the same as that of the downward

motion, because the same temperature stratification $N^2(z, t)$ is used for both sides. During the night, ascending motion occurs over the ocean and descending motion occurs over the land (Fig. 4b). The amplitude of the sea breeze circulation becomes weaker during the night than in the daytime, because of stable stratification in the lower atmosphere at night but nearly neutral stratification during the daytime. Notice that the internal gravity waves radiate from the coast in both Figs. 4a and 4b, becoming more evident during the night because of the weak sea breeze circulation and lower viscosity. The sea breeze circulation obtained here is consistent with that of previous studies. The internal gravity waves associated with the sea breeze circulation may not be well produced in some sea breeze models due to a very high viscosity or other artificial constraints. Their occurrence, however, is quite normal.

Results from 0200 LST of day 5 to 0200 LST of day 7 with a time interval of 12 h are shown in Fig. 5. At 0200 LST of day 5, the flow pattern near the coastline is a sea breeze circulation; i.e., downward motion on the landside and upward motion on the oceanside. The horizontal scale of the land-sea-breeze circulation is ~100 km. Strikingly, an opposite circulation with a stronger amplitude develops just outside the sea breeze circulation. The anti-sea breeze circulation also occurs at 1400 LST of day 5, completely disappears at 0200 LST and 1400 LST of day 6, and reappears at 0200 LST of day 7. The amplitude of the circulation gradually increases with time. The flow patterns in Fig. 5 can be explained by superposition of the two different circulations (Fig. 6). One circulation is the land-sea breeze with a horizontal wavelength 100 km, and the other is the wave related to trapeze instability, with a horizontal wavelength of 320 km. The period of the sea breeze is 24 h, but the period of the trapeze instability is 48 h. At 0200 LST and 1400 LST of day 5, these two waves are out of phase. Therefore, four cells appear in Fig. 5, and a similar situation happens at 0200 LST of day 7. But the sea breeze and trapeze wave are in phase at 0200 and 1400 LST of day 6, and therefore only a pair of cells occurs, with a considerably larger amplitude than those of day 5. The vertical wavelength is ~1.2 km, the horizontal wavelength is about 320 km, and the period is two days; these scales satisfy the well-known dispersion relation of inertial-gravity waves given by (3.5) for $f = 0$:

$$\sigma^2 = \frac{k^2N_0^2 + (m\pi/h)^2f^2}{k^2 + (m\pi/h)^2}. \qquad (3.5)^4$$

[4] This equation can be obtained by assuming $W_0 = W_{00}e^{i\sigma t}$, $N_1^2 = 0$, $C_1 = 1$, and $l = 0$ in (2.18).

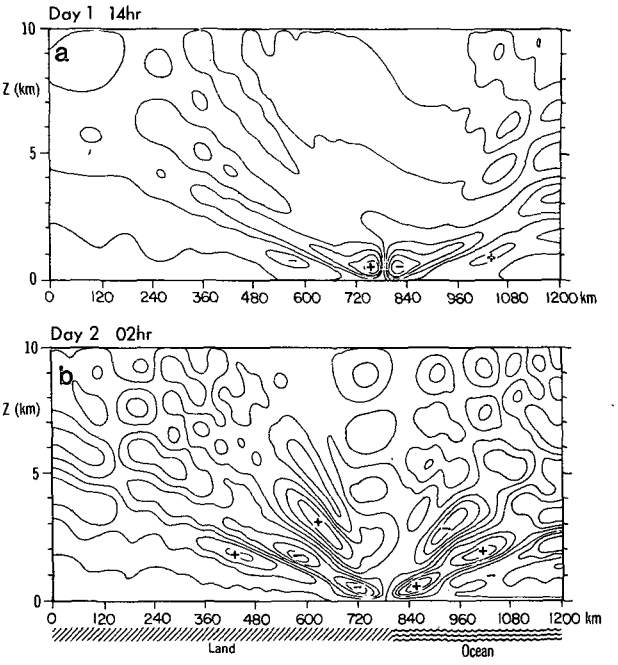

FIG. 4a. The vertical cross section of the vertical velocity w at 1400 LST of day 1 of case A. The maximum is 6.58 cm s^{-1}, the minimum is −6.67 cm s^{-1}, and the interval is 1.32 cm s^{-1}.

FIG. 4b. As in Fig. 4a except at 0200 LST of day 2. The maximum is 3.67 cm s^{-1}, the minimum is −3.78 cm s^{-1}, the interval is 0.75 cm s^{-1}.

It is interesting to point out that the opposite circulation shown on days 5 and 7 can be traced back even to day 1 in Fig. 4, although the amplitude is very weak at that time.

b. *Case B; $f = 0$*

The stratification over land is very different from that over the ocean as mentioned before. The satellite picture (Fig. 1) shows that clouds mainly develop over the continent, with much less cloud or even a clear sky over the ocean. Therefore, the more general equation (2.6), that includes the horizontal gradients of the stratification, will be used instead of (3.2) to solve for the z-velocity w, and (2.4) will be used to solve for potential temperature.

The coefficients for the basic potential temperature in (2.12) are the same as those given in case A except $B = (3.0 \times 10^6 \text{ cm})^{-1}$. The coefficients of viscosity in (3.3) are $\nu_0 = 4.63 \times 10^3$ cm^2 s^{-1}, $C_{\min} = 0.1$ and $\nu_x = 1.8 \times 10^3\nu_z$.

The results of the z-velocity field w from 1400 LST of day 14 to 1400 LST of day 16 with a time interval of 12 h are presented in Fig. 7. The potential energy of the trapeze instability is triggered by the sea breeze circulation. Therefore, the mesoscale wave develops near the coast, and these waves gradually grow and spread inland. The horizontal

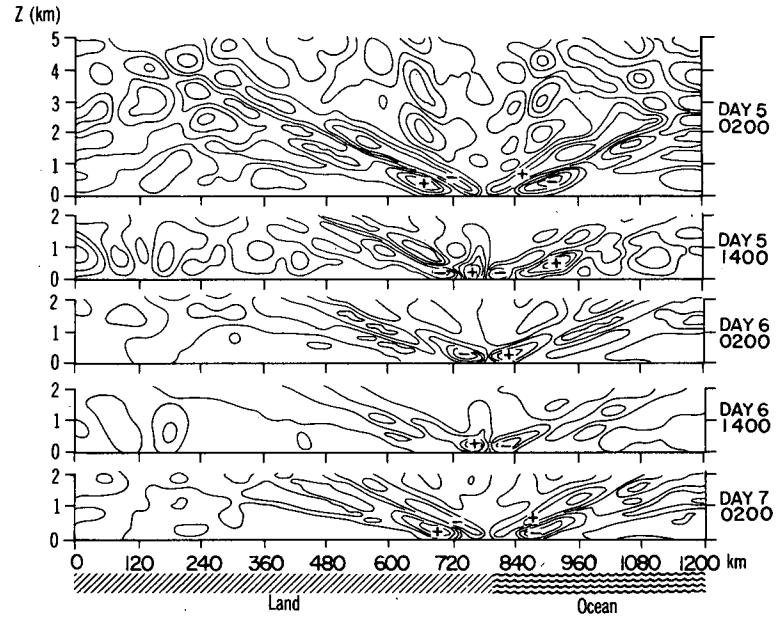

FIG. 5. A composite picture of the vertical velocity in the lower atmosphere from 0200 LST of day 5 to 0200 LST of day 7, at 12 h intervals. The maximum is 5.9 cm s^{-1} and the minimum -4.7 cm s^{-1} at 0200 LST of day 5; the maximum 10.6 cm s^{-1} and minimum is 8.7 cm s^{-1} at 1400 LST of day 5; the maximum 10.2 cm s^{-1} and minimum -10.3 cm s^{-1} at 0200 LST of day 6; the maximum 21.4 cm s^{-1} and minimum -20.4 cm s^{-1} at 1400 LST of day 6; the maximum 12.2 cm s^{-1} and minimum -11.7 cm s^{-1} at 0200 LST of day 7.

wavelength is about 380 km, the vertical wavelength is ~1.5 km and the period is two days. It can be seen from Fig. 7 that the 2-day waves even dominate the sea breeze circulation near the coast. The waves over the ocean are much weaker than those over land, because the amplitude of the diurnal variation of temperature over land is five times larger than that over the ocean. The magnitude of the vertical motion is about a few tens of centimeters per second on day 15.

The horizontal velocities at $z = 600$ m and at three different positions x_1 (=528 km), x_2 (=768 km) and x_3 (=1008 km) are shown in Fig. 8. The amplitude of u_2 grows very fast during the first day. u_2 has the period of one day for the first three days, then it becomes irregular until day 11. After that a period of two days becomes apparent for u_2.[5] The curve of u_1 seems very irregular during the first eight days, and then it becomes regular with a 2-day period, growing gradually. These 2-day waves can be traced back to the early days of the solution, since the local maxima can be found around 1800 LST of day 1, day 3, day 5 and day 7. The amplitude of u_1 is larger than that of u_2 after day 7. Since many internal gravity waves with different wavelengths and different growth rates are triggered by sea breezes during the first few days near the coast, they propagate away, interfering with one another and at the same time interacting with the sea breeze circulation. After eight days, the most unstable mode with a 2-day period becomes dominant over land. Because the horizontal scale of strong temperature gradients

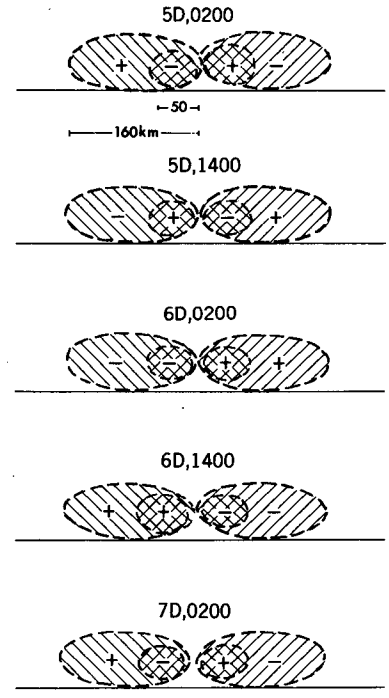

FIG. 6. A dramatic illustration of the superposition of 1- and 2-day waves corresponding to Fig. 5.

[5] The scale is changed at 1000 LST of day 10.

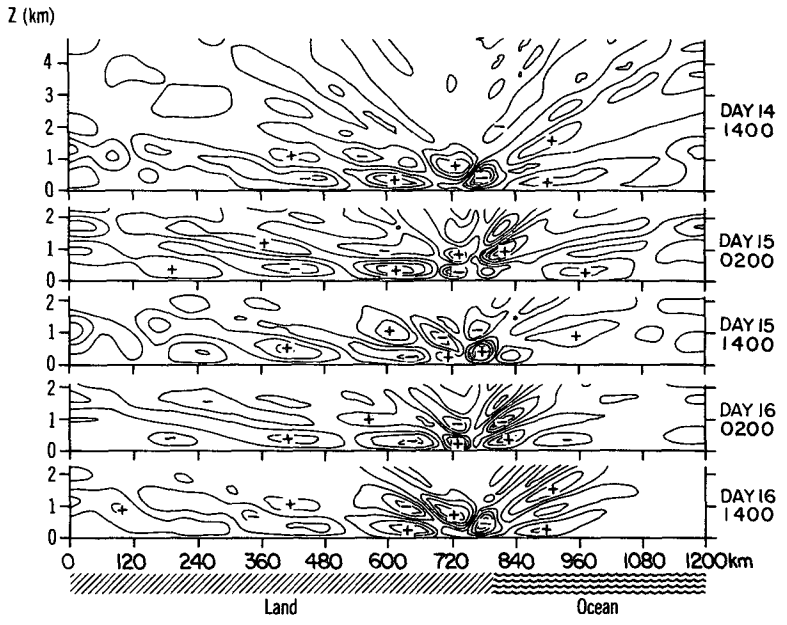

FIG. 7. A composite picture of the vertical velocity in the lower atmosphere from 1400 LST of day 14 to 1400 LST of day 16 at 12 h intervals for case B. The maximum is 20.1 cm s^{-1} and the minimum -32.4 cm s^{-1} at 1400 LST of day 14; the maximum 26.5 cm s^{-1} and minimum -24.4 cm s^{-1} at 0200 LST of day 15; the maximum 45.6 cm s^{-1} and minimum -21.6 cm s^{-1} at 1400 LST of day 15; the maximum 52.6 cm s^{-1} and minimum -42.4 cm s^{-1} at 0200 LST of day 16; the maximum 41.4 cm s^{-1} and minimum -51.8 cm s^{-1} at 1400 LST of day 16.

near the coast is only a few tens of kilometers, a sea breeze circulation occurs near the coast (Fig. 7). The u velocity over the ocean u_3 is much weaker than either u_1 or u_2. That may be used to justify the assumption $u = 0$ at the lateral boundary over the ocean. The 2-day waves obtained here seem qualitatively similar to the distribution of clouds in the West African continent during the night (Orlanski, 1976b). The downward motion at 1400 LST of day 14 is 32.4 cm s^{-1} and it increases to 51.8 cm s^{-1} at 1400 LST of day 16.

c. *Case C; $f = 0$*

The equations and boundary conditions applied in this case are exactly the same as those of case B.

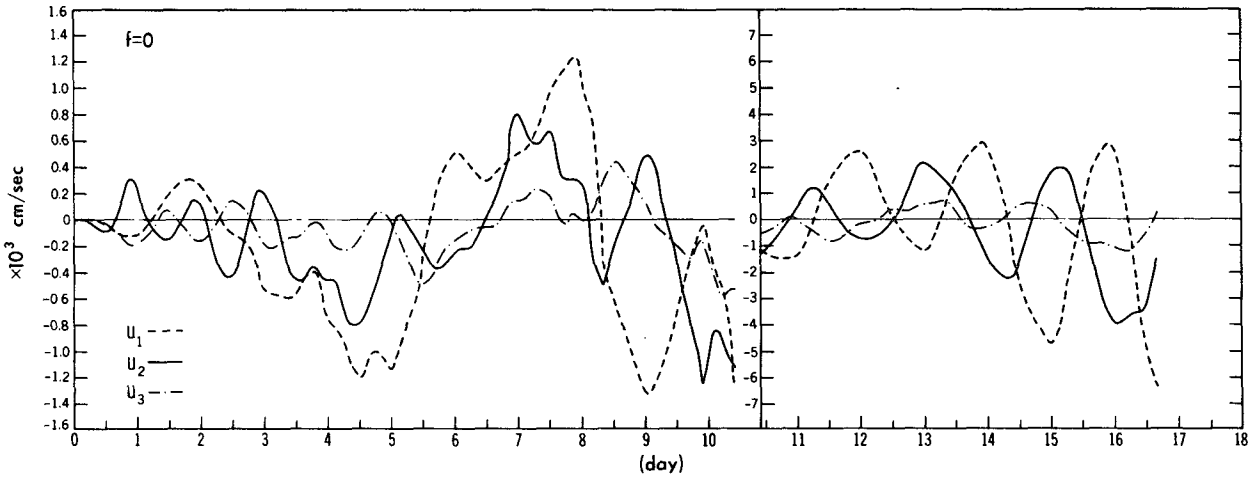

FIG. 8. The temporal variation of the x component velocity u_1 at 600 m at $x_1 = 528$ km (dashed line), of u_2 at $x_2 = 768$ km (solid line), and of u_2 at $x_2 = 1008$ km (dash-dotted line), from 0000 of day 0. The scale is changed at 1000 LST of day 10, after that the scale is five times as large as the scale used at beginning.

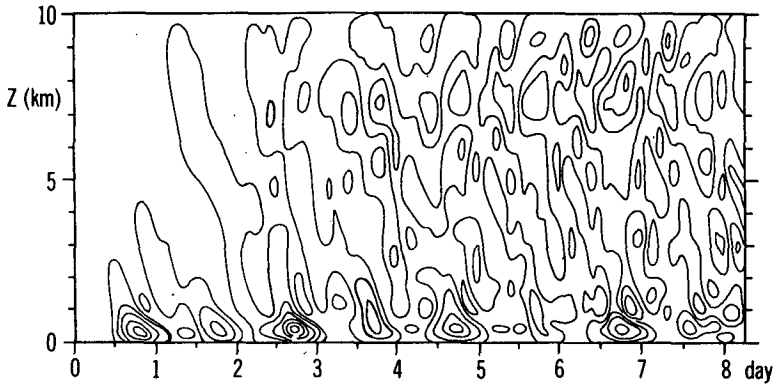

FIG. 9. The temporal variation of z velocity (w_2) at x = 768 km from 0000 LST of day 0 to 0600 LST of day 8 for case C. The maximum is 3.1 cm s^{-1}, the minimum −7.53 cm s^{-1}, and the interval is 1.06 cm s^{-1}.

The parameters are also the same as those in case B except here A = 1.0 and B = (6.0 × 10^6 cm)$^{-1}$. Therefore, the temperature does not have a diurnal variation over the ocean, and the temperature gradient across the coastline here is weaker than that in case B.

The temporal variation of w at x_2 = 768 km (w_2) at the height of 600 m from 0000 LST of day 0 to 0600 LST of day 8 is shown in Fig. 9, respectively. After a few days, the integration of the solution behaves as in the previous examples, with the 2-day period wave emerging as the most unstable mode. The temporal variation of x velocities at z = 600 m and x = 528 km (u_1), x = 768 km (u_2), and x = 1008 km (u_3) are shown in Fig. 10. The x-component velocity u_1 shows a period of two days from the beginning, and its amplitude increases considerably after day 6. The velocity u_2 at the coast has a diurnal variation corresponding to the sea breeze circulation in the first three days. Then the wave with a 2-day period grows very fast and becomes dominant after day 7. The velocity u_3 over the ocean is similar to u_2 except the amplitude of u_3 is smaller than u_2. It is noted that the energy of the weak waves over the ocean should come from the disturbances near the coast or over land, because there is no diurnal variation of stratification over the ocean. Nitta and Esbensen (1974) found that diurnal variation in velocity field existed in the Western Atlantic Trades during BOMEX, during which observations were made a few hundred kilometers from the coast. The maximum amplitude of the u and v components is ~1.5 m s^{-1}, due to a strong land-sea contrast, although the variation of the temperature at the sea surface is usually quite small.

The vertical cross sections of w at midnight (2400 LST) for days 6, 7, 8 and 9 are shown in Fig. 11a,

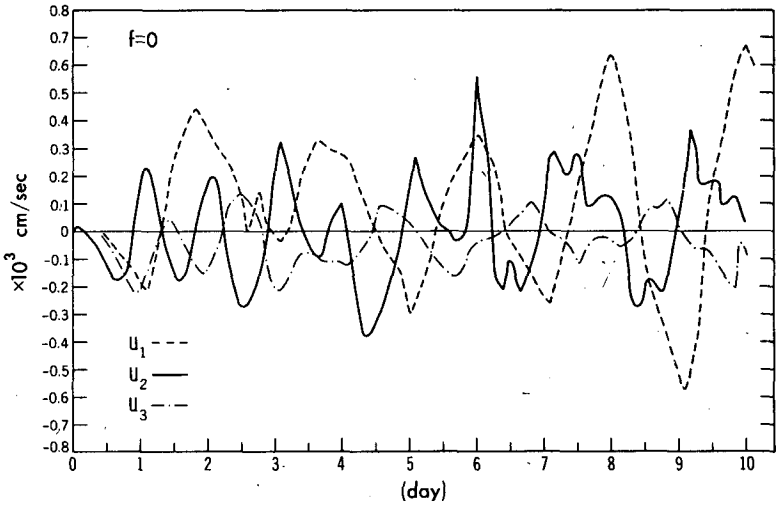

FIG. 10. The temporal variation of the x-component velocity u_1, u_2 and u_3 from the beginning to day 10 for case C.

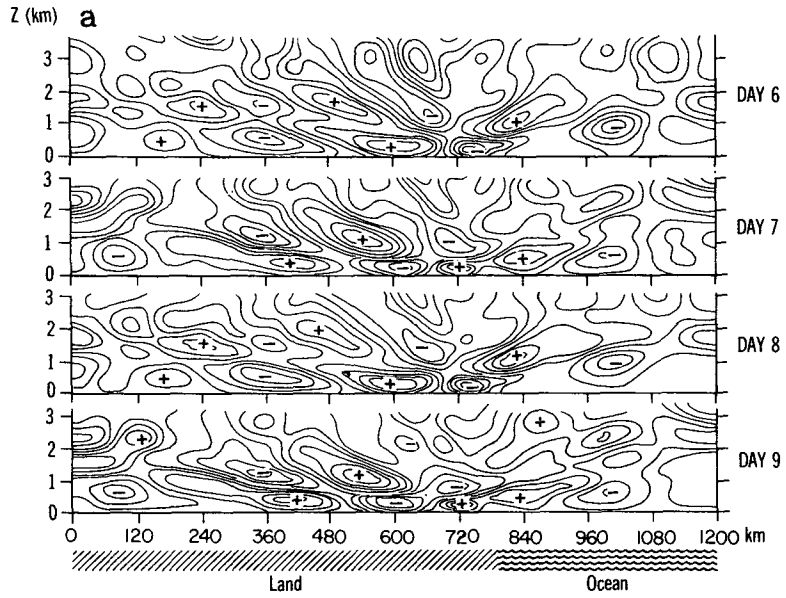

FIG. 11a. The vertical cross section of w at midnight (2400 LST) for day 6, 7, 8 and 9. The maximum is 3.29 cm s^{-1} and minimum -3.39 cm s^{-1} at 2400 LST of day 6; the maximum 3.80 cm s^{-1} and minimum -3.21 cm s^{-1} at 2400 LST of day 7; the maximum 4.63 cm s^{-1} and minimum -4.84 cm s^{-1} at 2400 LST of day 8; the maximum 3.98 cm s^{-1} and the minimum -4.73 cm s^{-1} at 2400 LST of day 9. (2400 of day 6 = 0000 of day 7).

while the field at 1600 LST is shown in Fig. 11b. In addition to the 1-day wave, the 2-day wave grows rapidly and clearly shows up near the ground surface in Fig. 11a. In the upper PBL, the amplitude also shows a 2-day fluctuation, but the fluctuation is not large enough to change the sign there. This

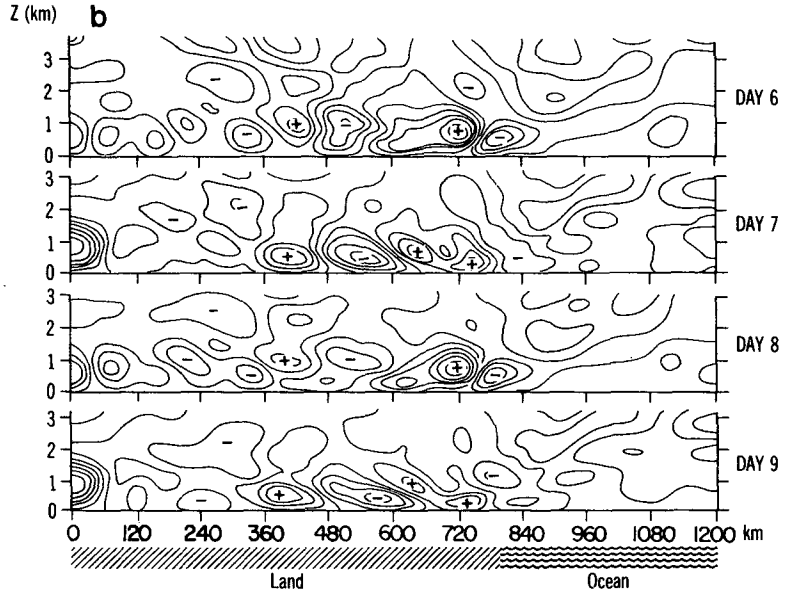

FIG. 11b. A composite of the vertical cross section of the w velocity at 1600 LST of day 6, 7, 8 and 9. The maximum is 5.85 cm s^{-1} and minimum -4.58 cm s^{-1} at 1600 LST of day 6; the maximum 4.87 cm s^{-1} and minimum -6.87 cm s^{-1} at 1600 LST of day 7; the maximum 7.92 cm s^{-1} and minimum -6.11 cm s^{-1} at 1600 LST of day 8; the maximum 5.83 cm s^{-1} and minimum -9.14 cm s^{-1} at 1600 LST of day 9.

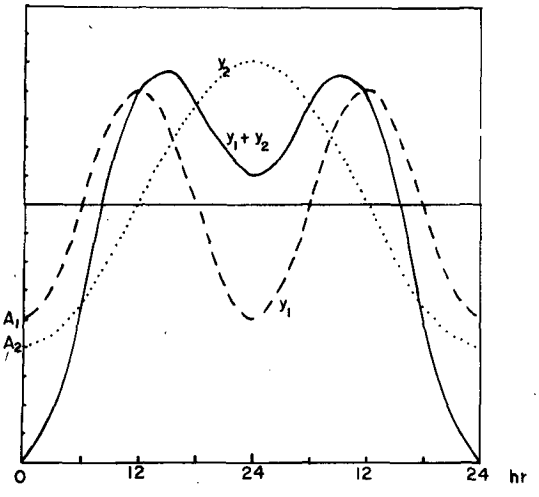

FIG. 12. The fluctuations of 1-day waves y_1, 2-day waves y_2, and the summation of y_1 and y_2.

phenomenon can be explained by a superposition of the 1-day and 2-day unstable waves. According to (3.5), the vertical wavelength of the 1-day period waves is twice that of the 2-day period waves, if their horizontal wavelengths are the same. Here the horizontal wavelength is ~360 km and the vertical wavelength is ~1.5 km for 2-day period waves, but it is ~3.0 km for 1-day period waves. The amplitude becomes large in the area where 2-day period waves and 1-day period waves are in phase, but it becomes small where those waves are out of phase.

Now, let us look at the w fields at 1600 LST for days 6, 7, 8 and 9 (Fig. 11b). The differences between the solutions at 0000 and 1600 LST are quite obvious; the 1-day wave is as important as the 2-day wave. The waves are less regular during the daytime than at night. This phenomenon is consistent with that observed in the satellite pictures presented and discussed by Orlanski (1976b). If we define the fluctuations of 1-day and 2-day waves as follows:

$$y_1 = A_1 \cos \frac{2\pi(t - 12\text{ h})}{24\text{ h}},$$

$$y_2 = A_2 \cos \frac{2\pi(t - 24\text{ h})}{48\text{ h}}. \qquad (3.6)$$

Here A_1 is the amplitude of the 1-day wave and $A_2(>A_1)$ is the amplitude of the 2-day wave as shown in Fig. 12. Although A_2 is greater than A_1, the fluctuation of y_2 is smaller during the daytime hours when y_1 is maximum, so 1-day wave will show up more clearly during the daytime. But $y_1 + y_2$ shows a clear 2-days oscillation during the night.

d. Case D; $f = 0$

The equations and boundary conditions applied in this case are exactly the same as those of case C

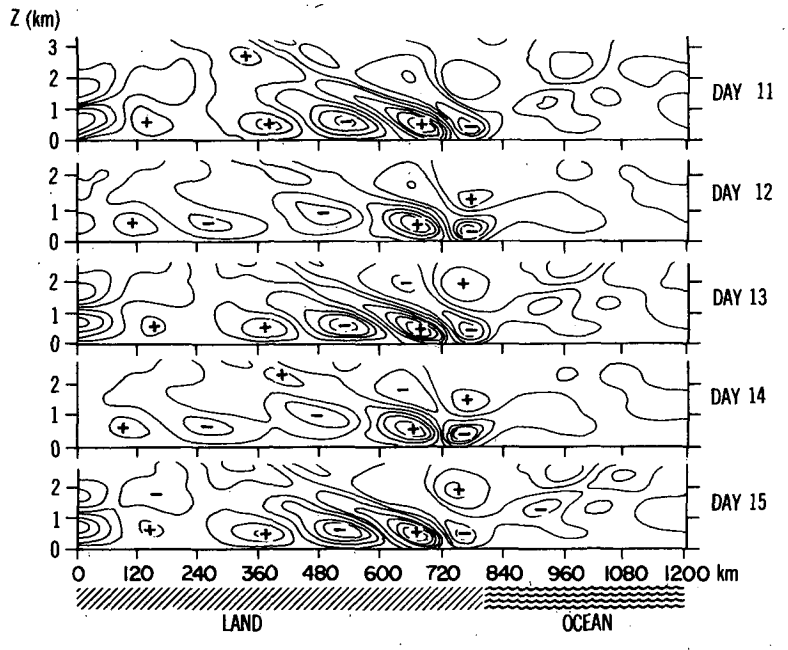

FIG. 13. A composite of the vertical cross section of w at 2000 LST from day 11 to 15 for case D. The maximum is 5.28 cm s^{-1} and minimum −4.79 cm s^{-1} at 2000 LST of day 11; the maximum 7.35 cm s^{-1} and minimum −8.84 cm s^{-1} at 2000 LST of day 12; the maximum 6.78 cm s^{-1} and minimum −5.93 cm s^{-1} at 2000 LST of day 13; the maximum 9.08 cm s^{-1} and minimum −10.6 cm s^{-1} at 2000 LST of day 14; the maximum 7.54 cm s^{-1} and minimum −6.39 cm s^{-1} at 2000 LST of day 15.

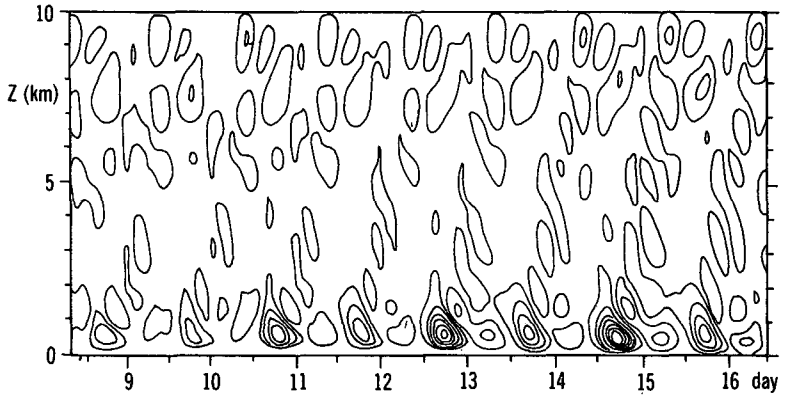

FIG. 14. Temporal variation w_2 from 0600 LST of day 8 to 1200 LST of day 16. The maximum is 3.55 cm s^{-1} and minimum -1.19 cm s^{-1}. The interval is 1.55 cm s^{-1}.

except the viscosity here is five times greater than that of case C during the night; i.e., $C_{\min} = 0.5$ instead of 0.1 used in case C. The vertical velocity field at 2000 from day 11–15 is shown in Fig. 13. The effect of increasing ν_z shows in the increase of λ_z, λ_z is ~2.5 km here which is almost twice as large as that in case C. The horizontal wavelength λ_x is not affected due to the change of ν_x, because the Shuman smoothing applied in the horizontal direction is more important than the horizontal diffusion term in the momentum equations.

For a horizontal wavelength $\lambda_x = 300$ km and a vertical wavelength $\lambda_z = 2.4$ km, the 1-day wave is more suitable than the 2-day wave, according to the dispersive relation given by (3.5). It is not difficult to see, however, the existence of the 2-day wave with horizontal wavelength $\lambda_{x\,(2\text{-day})} = 2\lambda_{x\,(1\text{-day})}$ at the same time. It can also be found in the time sequence of w in Fig. 14 at $x_2 = 768$ km (from 0600 LST of day 8 to 1200 LST of day 16). This is similar to Fig. 9 for case C.

Here the 2-day wave cannot dominate the 1-day wave as in the previous cases, because the horizontal length scale of the forcing (i.e., the temperature gradient zone in the coastal area) is only a few tens of kilometers. This is closer to $\lambda_{x\,(1\text{-day})}$ and since $\lambda_{x(1\text{-day})} = 0.5\lambda_{x(2\text{-day})}$. Thus, waves with a small horizontal wavelength may be easily excited by the sea breeze circulation.

e. Case E, $f = 0.333 \times 10^{-4}$ s^{-1} (13.24°N)

The equations and the parameters are exactly the same as those in case B except now the Coriolis parameter is $f = 0.333 \times 10^{-4}$ s^{-1} (corresponding to 13.24°N) and $B = (30\text{ km})^{-1}$ and $C_{\min} = 0.1$. The time sequence of the u_1, u_2 and u_3 at a height of 600 m are presented in Fig. 15. The combination

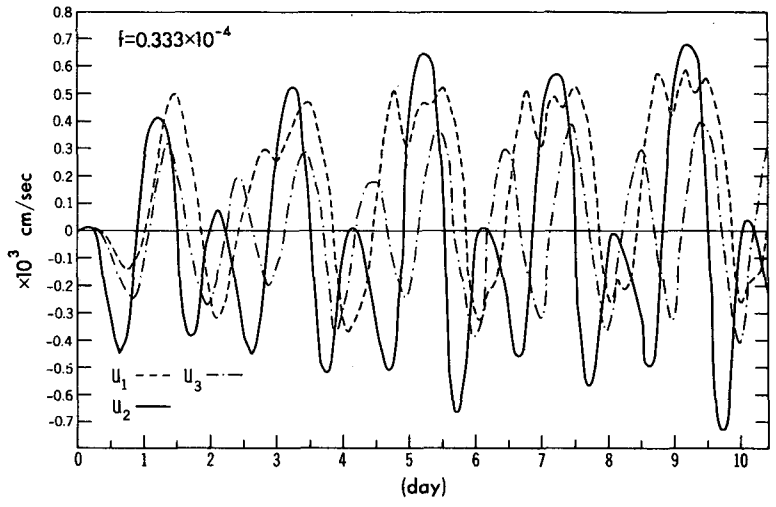

FIG. 15. The velocities u_1, u_2 and u_3 at 600 m for case E.

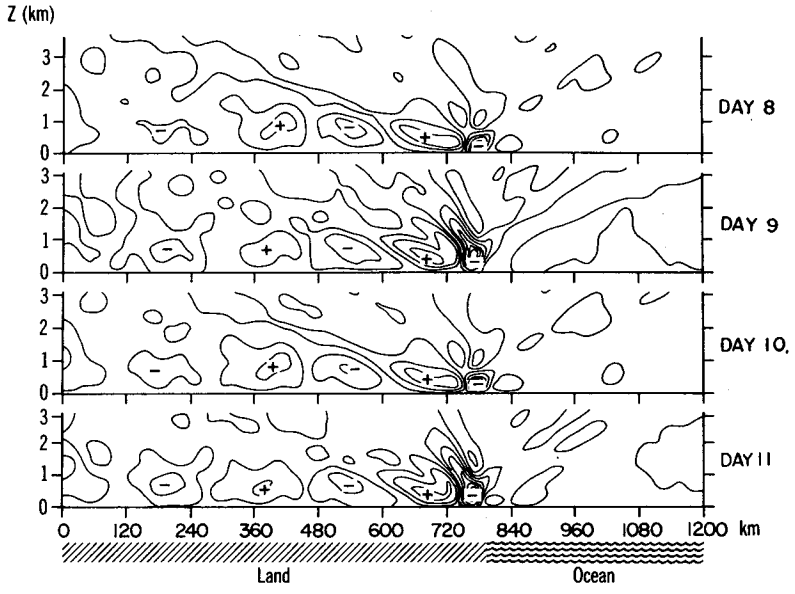

FIG. 16. The vertical cross section of w at 1800 LST of day 8, 9, 10 and 11. The maximum is 8.77 cm s^{-1} and minimum -18.1 cm s^{-1} at 1800 LST of day 8; the maximum 9.70 cm s^{-1} and minimum -15.4 cm s^{-1} at 1800 LST of day 9; the maximum 9.86 cm s^{-1} and minimum -20.4 cm s^{-1} at 1800 LST of day 10; the maximum of 10.6 cm s^{-1} and minimum -18.4 cm s^{-1} at 1800 LST of day 11.

of 1-day waves and 2-day waves clearly appears in u_2 and u_3, which is similar to the curve of $y_1 + y_2$ in Fig. 12. Here the shape of the curves is more regular and the growth rate is smaller than those of case B. The time sequences of the vertical velocities w_1 and w_2 (not shown here) show that the 1-day wave is much clearer than 2-day period wave. This is also true in the vertical cross section of w for 1800 LST of days 8, 9, 10 and 11, shown in Fig. 16. According to the dispersive relation given in (3.5), when the vertical wavelength is ~2.6 km, the horizontal wavelength will be ~380 km for the 1-day wave. When the vertical wavelength is 3.0 km, the horizontal wavelength will be 2000 km for the 2-day wave. Therefore it is reasonable to expect that the 1-day wave will develop faster in this case. Our results are consistent with the organized squall lines which produce a diurnal variation of rainfall in large areas of tropical West Africa, as discussed in detail by McGarry and Reed (1978), and others. It is noted that the 2-day period is more easily observed than the 1-day period in the x-velocity field than in the z-velocity component, as shown in Figs. 14 and 15. This phenomenon is also found in Orlanski's nonlinear model (see Figs. 10 and 11 of Orlanski, 1976) and our numerical result in Part II of this paper.

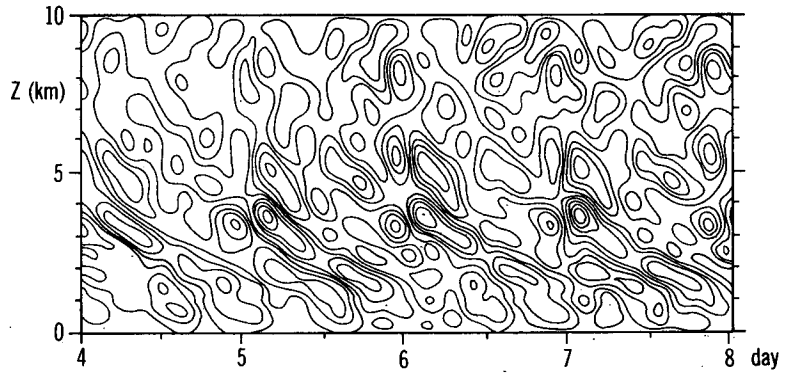

FIG. 17. The time sequence of the vertical velocity at x = 1008 km from 0300 LST of day 4 to 0700 LST of day 8. The maximum is 4.55 cm s^{-1}, the minimum -3.38 cm s^{-1} and the interval 0.79 cm s^{-1}.

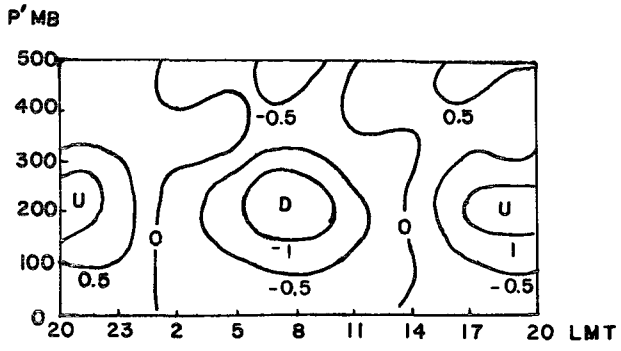

FIG. 18. Diurnal variation of vertical P' velocity during BOMEX. P' = pressure at surface − pressure at the level (after Nitta and Esbensen, 1974).

The time sequence of the vertical velocity at $x = 1008$ km is presented in Fig. 17 from 0300 LST of day 4 to 0700 LST of day 8. The maximum amplitude of the diurnal variation occurs at $z = 3400$ m. The amplitude near the ground surface is quite weak. This phenomenon was in qualitative agreement with the data obtained by Nitta and Esbensen (1974) and presented in Fig. 18, in which the amplitude reaches its peak ~2500 m. The BOMEX observations were made a few hundred kilometers from the coast, at around latitude 15°N, which is comparable with the case discussed here. Nitta and Esbensen concluded that the diurnal variation observed during BOMEX came from the strong land-sea contrast a few hundred kilometers away, since the amplitude observed is nearly one order of magnitude larger than that obtained by tide theory proposed by Lindzen (1967) and Hastenrath (1972). We would also like to point out that the phase speed of the waves in Fig. 17 propagates downward, which is consistent with that obtained by Orlanski (1973), as well as Kuo and Sun (1976). Since the energy comes from the sea breeze circulation in the lower mixed layer near the coastal region, the group velocity of the internal gravity waves propagates upward. But a change of the phase angle with height is not clear in Fig. 18. This may come from the change of prevailing wind with height or the large horizontal area over which the observational data is averaged.

f. Case F; $f = 0.727 \times 10^{-4}\ s^{-1}$ (30°N)

The parameters and the equations used here are the same as those in case E except the Coriolis parameter is $f = 0.727 \times 10^{-4}\ s^{-1}$ (corresponding to 30°N), $B = 1.0/30$ km, and $C_{min} = 0.1$. The inertial period is exactly one day at this latitude. The temporal variation of u_1, u_2 and u_3 (Fig. 19) shows a familiar 1-day period in three different locations. From this figure, we also know that the wind blows from the ocean to the land during the daytime, and from the land to the ocean during the night. The vertical cross section of w presented in Fig. 20 show that the sea breeze circulation develops near the coast. The center of the sea breeze moves inland ~25 km at 1400 LST, because the wind comes from the ocean. But it moves off land about 25 km at midnight, because the wind comes from the land at that time. This is consistent with observations. Referring back to Figs. 4 and 5, we find the center of the sea breeze is fixed in case A, since the horizontal advection term is ignored in that case. In addition to the sea breeze, Fig. 20 reveals many internal gravity waves radiating from the coast. Some of them cannot go through the lateral or upper boundaries, so they are reflected and reach the ground surface near $x = 150$ km. If we ignore this point, a weak unstable wave can be found on both sides of the coast with a wavelength larger than the

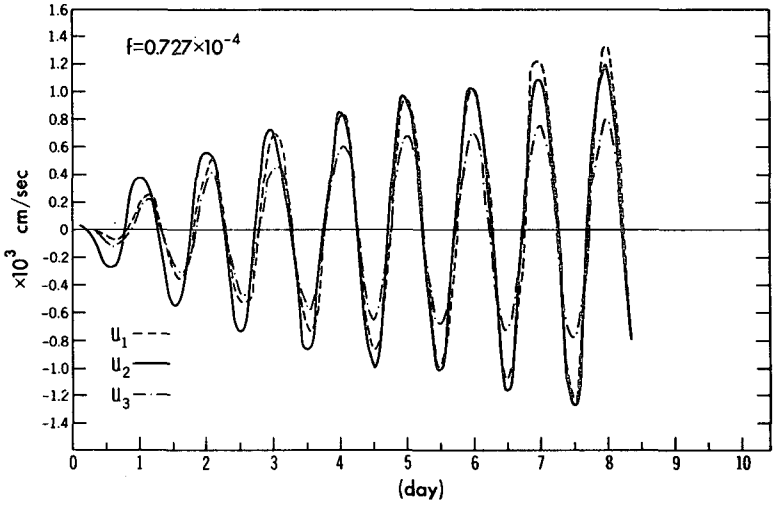

FIG. 19. The temporal variation of u_1, u_2 and u_3 from the beginning of day 8 for case F.

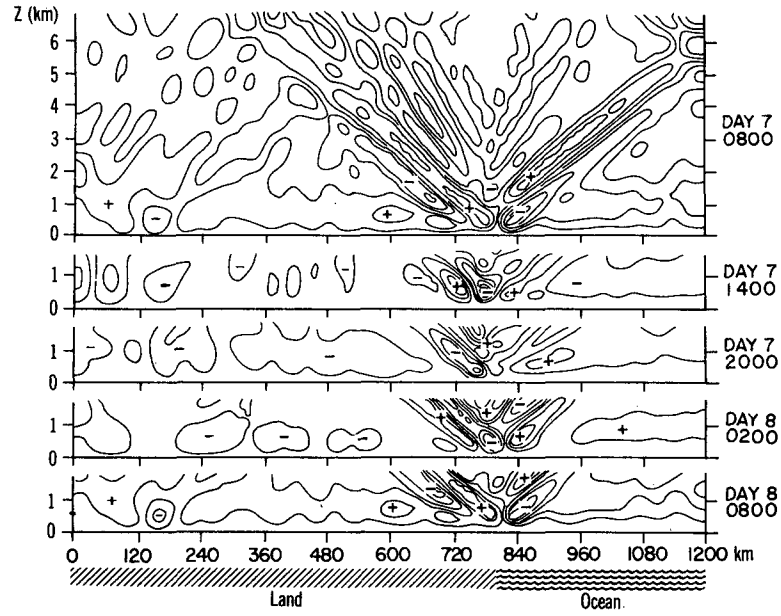

FIG. 20. A composition of the vertical cross section of w from 0800 LST of day 7 to 0800 LST of day 8 for an interval of 6 h. The maximum is 4.66 cm s^{-1} and minimum -5.89 cm s^{-1} at 0800 LST of day 7; the maximum 7.68 cm s^{-1} and minimum -13.1 cm s^{-1} at 1400 LST of day 7; the maximum 6.47 cm s^{-1} and minimum -10.8 cm s^{-1} at 2000 LST of day 7; the maximum 5.07 cm s^{-1} and minimum -8.18 cm s^{-1} at 0200 LST of day 8; the maximum 5.07 cm s^{-1} and minimum -6.18 cm s^{-1} at 0800 LST of day 8.

domain (1200 km) and of 1-day period. This is just an inertial-internal gravity wave with a very small growth rate. The horizontal scale of the sea breeze is ~100 km and the vertical wavelength is ~1.4 km. From the dispersive relation given by (3.5), we can expect a 12 h period wave in this region too. This can be clearly seen from the time sequence of w_2 (Fig. 21), although the amplitude of the 12 h period wave is weaker than that of the diurnal wave, as expected.

g. Case G; $f = 1.0 \times 10^{-4}$ s^{-1} (near 45° latitude)

The equations and the parameters used here are the same as those in case F except the Coriolis parameter is $f = 1.0 \times 10^{-4}$ s^{-1} (corresponding to 43.5°N). The time sequence of u_1, u_2 and u_3 is shown in Fig. 22. A quasi-steady wave occurs at those three locations. A large amplitude of u_2 corresponds to the sea breeze circulation. A very small amplitude of u_1 shows no unstable waves associated with the diurnal variation of stratification, since the damping effect from the Coriolis force is too strong to allow trapeze instability to operate.

4. Summary

The interaction between trapeze instability and the sea breeze circulation has been investigated by a linear model. The results show that the growth rate, wavelength and period are strongly dependent on the Coriolis parameter, the eddy viscosity, the horizontal scale of land-sea contrast, and the amplitude of the diurnal variation of the temperature. The cases studied are summarized in Table 1. At the equator, when the viscosity is small and the length

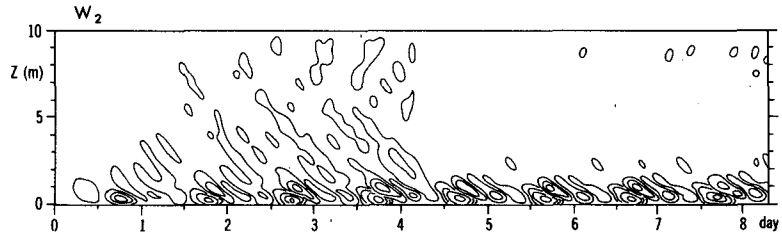

FIG. 21. Time sequence of w_2 from the beginning to 0700 LST of day 8. The maximum is 9.53 cm s^{-1} and minimum -17.3 cm s^{-1}.

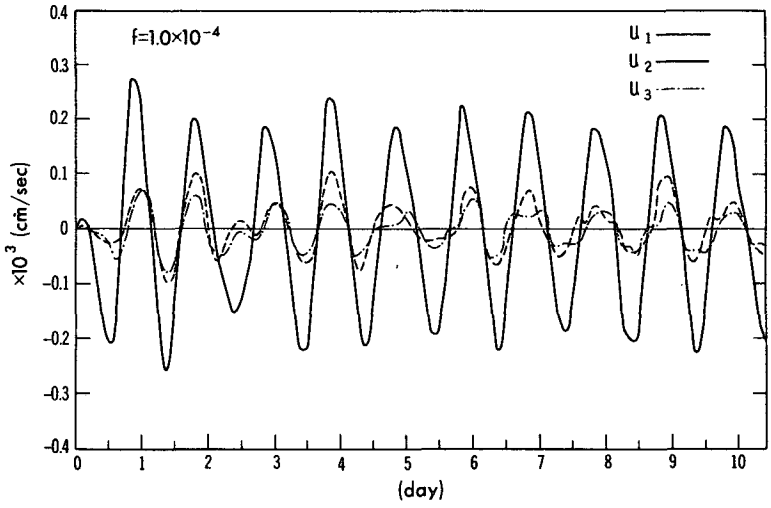

FIG. 22. The time sequence of u_1, u_2 and u_3 at 600 m for case G.

scale of land-sea contrast is small, the wave with a 2-day period becomes the most unstable over land. The potential energy of the trapeze instability is triggered by the sea breeze circulation, and the waves start to develop near the coast, with organized cloud bands spreading far inland. There is no organized cloud band over the ocean according to results from case B. When the horizontal scale of land-sea contrast increases, the 2-day wave can no longer dominate the 1-day wave. Therefore, the coexistence of 1-day and 2-day waves show up in our results. The 2-day waves show up more clearly during the night, but 1-day waves appear more clearly during the daytime. This is consistent with the satellite pictures discussed by Orlanski (1976b). When the viscosity increases, the 1-day wave may become as important as, or even more important than, the 2-day wave, based on the results of case D.

When the Coriolis force is $f = 0.333 \times 10^{-4}$ s^{-1}, the results from case E show that over the land, 1-day waves clearly appear in the vertical velocity field. However, 1-day waves and 2-day waves coexist in the horizontal component of velocity, just as in the nonlinear numerical results obtained by Orlanski. A 1-day wave with a maximum amplitude near 3000 m can be observed in the temporal variation of the z-component velocity a few hundred kilometers off the coast; this is in good agreement with the data observed during BOMEX by Nitta and Esbensen. They concluded that the diurnal variation at BOMEX was caused by a strong land-sea contrast.

When $f = 0.727 \times 10^{-4}$ s^{-1}, the results from case F tell us that the period of the waves is equal to or less than one day, which is consistent with the dispersive relation of an internal-inertial wave at a latitude >30°. The growth rate becomes smaller as f increases.

When $f = 1.0 \times 10^{-4}$ s^{-1}, the sea breeze circulation and some short-period waves exist near the coast. No instability occurs here, due to the large damping effect associated with large f.

The theoretical results obtained in the equatorial and low latitude region (i.e., $f \leq 0.333 \times 10^{-4}$ s^{-1}) confirms that the 1-day and 2-day waves can be easily produced by the interaction between trapeze instability and the sea breeze circulation. The flow will become organized into mesoscale waves near the coast, and then these waves will spread inland with a horizontal length scale of ~300–600 km and the depth of the planetary boundary layer ~2 km. But no significantly organized waves are found over the ocean in our numerical results.

All of these are consistent with the spectral analysis of the cloudiness over Africa and GATE region of Orlanski and Polinsky (1977), and with the satellite picture presented in Fig. 1. These waves can reach finite amplitude within a few days, because the equations are inhomogeneous. Therefore, the release of the local potential energy of trapeze

TABLE 1. The letters show the circulations we obtained from the corresponding cases, and the bar above letter indicates the dominate one. "Sea breeze only" indicates that the circulation is mainly associated with the land-sea breeze circulation.

Period ($f \times 10^4$ s)	6 h	12 h	24 h	48 h	Comment on mesoscale waves
0.0			A*	Ā	unstable
0.0			B*	B̄	unstable
0.0			C	C	unstable
0.0			D̄	D	unstable
0.333			E	E	less unstable
0.727		F	F̄		very weak, unstable
1.0	G	G	Ḡ*		stable

* Seabreeze only.

instability can effectively be triggered by the sea breeze circulation in this simulation, unlike the homogeneous case investigated by Orlanski (1973). Another important difference is that the horizontal length scale can be determined independently in this model. Waves with different wavelengths and periods can also coexist here, which may show a clear 2-day wave during the night but a 1-day wave during the daytime, as observed in the real atmosphere.

Some of the solutions presented here have been reproduced by a fully nonlinear numerical model with improved boundary conditions. These results will be presented as Part II of this study.

Acknowledgments. It is a pleasure to thank Dr. B. Ross and Mr. R. Shaginaw of G.F.D.L. for many useful discussions when the senior author was there. We also would like to thank Dr. Agee and Dr. Hong of Purdue University and anonymous reviewers for reading the manuscript and for comments which helped to clarify the paper.

APPENDIX A

List of Symbols

A	constant relative to the temperature contrast across the coast [cf. (2.13)]
B	constant relative to the length scale of strong temperature zone across the coast [cf. (2.13)]
C_1	$C_1 = 0$ for hydrostatic approximation; $C_1 = 1$ for nonhydrostatic approximation [cf. (2.3)]
C_2	constant $[=N_0^2/(A+1)]$
C_3	constant relative to the depth of boundary layer [cf. (2.13)]
f	Coriolis parameter
g	gravity acceleration
G_1, G_2	arbitrary constants [cf. (3.4)]
h	height of boundary layer
i, j	grid-point index in x and z direction, respectively
k, l	wavenumber along x and y direction, respectively
N^2, N_0^2, N_1^2	Brunt-Väisälä frequencies [cf. (2.13) and (3.2)]
p'	perturbation pressure
S_h	coefficient of Shuman's smoothing
t	time
t_0	2 h
u', v', w'	perturbation velocity in x, y and z direction
u_1, u_2, u_3	$u_1 = u$ (528 km, 600 m), $u_2 = u$ (768 km, 600 m), $u_3 = u$ (1008 km, 600 m)
w_1, w_2, w_3	$w_1 = w$ (528 km, 600 m), $w_2 = w$ (768 km, 600 m), $w_3 = w$ (1008 km, 600 m)
x_0	location of coast
z_0	height of the mixing layer
α	specific volume
$\theta, \tilde{\theta}, \theta', \bar{\theta}$	total potential temperature, environmental potential temperature, perturbation potential temperature and horizontal potential temperature, respectively $[\theta = \tilde{\theta} + \theta']$
ν_x, ν_z	eddy viscosity in x and z direction, respectively
ϕ	defined in (2.8)
∇^2	$= \dfrac{\partial^2}{\partial x^2} + \dfrac{\partial^2}{\partial z^2}$
∇_H^2	$= \dfrac{\partial^2}{\partial x^2} + \dfrac{\partial^2}{\partial y^2}$
$\nu\nabla^2$	$= \nu_x \dfrac{\partial^2}{\partial x^2} + \nu_z \dfrac{\partial^2}{\partial z^2}$
ω	angular velocity of the earth rotation.

APPENDIX B

The Equations

The complete form of heat equation should be

$$\frac{\partial(\tilde{\theta}+\theta')}{\partial t} + u'\frac{\partial(\tilde{\theta}+\theta')}{\partial x} + w'\frac{\partial(\tilde{\theta}+\theta')}{\partial z} = \frac{\partial\tilde{\theta}_*}{\partial t} + \nu\nabla^2(\tilde{\theta}+\theta'), \quad \text{(B1)}$$

where $\partial\tilde{\theta}_*/\partial t$ is an internal heating source (or sink). Eq. (B1) can be separated into two equations; one is for basic state

$$\frac{\partial\tilde{\theta}}{\partial t} = \frac{\partial\tilde{\theta}_*}{\partial t} + \nu\nabla^2\tilde{\theta} \simeq \frac{\partial\tilde{\theta}_*}{\partial t} \quad \text{(B2)}$$

and the other is for the linearized perturbation potential temperature

$$\frac{\partial\theta'}{\partial t} + u'\frac{\partial\tilde{\theta}}{\partial x} + w'\frac{\partial\tilde{\theta}}{\partial z} = \nu\nabla^2\theta'. \quad \text{(B3)}$$

Eq. (B3) is identical to (2.4).

The fundamental equations in three dimensions are

$$\left(\frac{\partial}{\partial t} - \nu\nabla^2\right)\mathbf{V}' + f\mathbf{K}\times\mathbf{V}' = \nabla_H P', \quad \text{(B4)}$$

$$C_1\left(\frac{\partial}{\partial t} - \nu\nabla^2\right)w' = -\frac{\partial P'}{\partial z} + g\alpha(\tilde{\theta}+\theta'-\bar{\theta}), \quad \text{(B5)}$$

$$\left(\frac{\partial}{\partial t} - \nu\nabla^2\right)\theta' = -u'\frac{\partial\tilde{\theta}}{\partial x} - w'\frac{\partial\tilde{\theta}}{\partial z}, \quad \text{(B6)}$$

$$\nabla_H \cdot \mathbf{V}' + \frac{\partial w'}{\partial z} = 0, \tag{B7}$$

where

$$\left.\begin{aligned} \nabla_H &= \mathbf{i}\frac{\partial}{\partial x} + \mathbf{j}\frac{\partial}{\partial y}, \\ \nabla^2 &= \frac{\partial^2}{\partial x^2} + \frac{\partial^2}{\partial y^2} + \frac{\partial^2}{\partial z^2} \\ \nu\nabla^2 &= \nu_x\frac{\partial^2}{\partial x^2} + \nu_y\frac{\partial^2}{\partial y^2} + \nu_z\frac{\partial^2}{\partial z^2} \end{aligned}\right\}.$$

From (B4) we can obtain the curl of $\mathbf{V}'$, i.e.,

$$\left(\frac{\partial}{\partial t} - \nu\nabla^2\right)\nabla_H \times \mathbf{V}' - f\mathbf{K}\frac{\partial w'}{\partial z} = 0. \tag{B8}$$

From (B5) we obtain

$$C_1\left(\frac{\partial}{\partial t} - \nu\nabla^2\right)\nabla_H w' = -\nabla_H\left(\frac{\partial P'}{\partial z}\right) + \nabla_H[g\alpha(\tilde{\theta} + \theta' - \bar{\theta})]. \tag{B9}$$

Then we take a vertical derivative of (B4), i.e.,

$$\left(\frac{\partial}{\partial t} - \nu\nabla^2\right)\frac{\partial \mathbf{V}'}{\partial z} + f\mathbf{K} \times \frac{\partial \mathbf{V}'}{\partial z} = -\nabla_H\left(\frac{\partial P'}{\partial z}\right) = C_1\left(\frac{\partial}{\partial t} - \nu\nabla^2\right)\nabla_H w' - \nabla_H[g\alpha(\tilde{\theta} + \theta' - \bar{\theta})]. \tag{B10}$$

If we apply the operator $\nabla_H \cdot$ on (B10), we obtain

$$\left(\frac{\partial}{\partial t} - \nu\nabla^2\right)\left(-\frac{\partial^2 w}{\partial z^2}\right) - f\mathbf{K}\cdot\nabla_H \times \frac{\partial \mathbf{V}'}{\partial z} = C_1\left(\frac{\partial}{\partial t} - \nu\nabla^2\right)\nabla_H{}^2 w' - \nabla_H{}^2\{g\alpha(\theta' + \tilde{\theta} - \theta)\}. \tag{B11}$$

Then operator $(\partial/\partial t - \nu\nabla^2)$ is applied in (B11). By using (B6) and (B8), we obtain

$$\left(\frac{\partial}{\partial t} - \nu\nabla^2\right)^2\left[\frac{\partial^2 w'}{\partial z^2} + C_1\nabla_H{}^2 w'\right] + f^2\frac{\partial^2 w'}{\partial z^2} = g\alpha\nabla_H{}^2\left(-w'\frac{\partial \tilde{\theta}}{\partial z} - u'\frac{\partial \tilde{\theta}}{\partial x} + \frac{\partial \tilde{\theta}}{\partial t}\right). \tag{B12}$$

If there is no perturbation along the y direction, Eq. (B12) becomes (2.6). If $\tilde{\theta} = \bar{\theta}$ and $\nu = 0$ are applied in (B4)–(B7), Eq. (B12) will become (2.16).

REFERENCES

Blackadar, A. K., 1957: Boundary layer wind maxima and their significance for the growth of nocturnal inversions. *Bull. Amer. Meteor. Soc.*, **38**, 283–290.

Buajitti, K., and A. K. Blackadar, 1957: Theoretical studies of diurnal wind structure variations in the planetary boundary layer. *Quart. J. Roy. Meteor. Soc.*, **83**, 486–500.

Cocheme, J., and P. Franquin, 1967: An agroclimatology survey of a semiarid area in Africa south of the Sahara. WMO Tech. Note No. 86, 136 pp.

Hastenrath, S., 1972: Daily wind, pressure, and temperature variation up to 30 km over the tropical western Pacific. *Quart. J. Roy. Meteor. Soc.*, **98**, 48–59.

Ing, G., 1971: Summer circulation and weather over the Korat Plateau, Thailand. Sci. Rep. No. 1, Contract F 19628-71-C-0072, Dept. of Meteorology, University of Hawaii, 41 pp.

Kuo, H. L., and W. Y. Sun, 1976: Convection in the lower atmosphere and its effects. *J. Atmos. Sci.*, **33**, 21–40.

Lindzen, R. S., 1967: Thermally driven diurnal tide in the atmosphere. *Quart. J. Roy. Meteor. Soc.*, **93**, 18–42.

Kousky, V. E., 1980: Diurnal rainfall variation in northeast Brazil. *Mon. Wea. Rev.*, **108**, 488–498.

Mak, M. K., and J. E. Walsh, 1976: On the relative intensities of sea and land breeze. *J. Atmos. Sci.*, **33**, 242–251.

Martin, D. W., 1975: Characteristics of West Africa and Atlantic cloud clusters. GATE Rep. No. 14, WMO, 182–190.

McGarry, M. M., and R. J. Reed, 1978: Diurnal variations in convective activity and precipitation during phase II and III of GATE. *Mon. Wea. Rev.*, **106**, 101–113.

Nitta, T., and S. Esbensen, 1974: Diurnal variations in the western Atlantic trades during the BOMEX. *J. Meteor. Soc. Japan*, **52**, 254–257.

Orlanski, I., 1973: Trapeze instability as a source of internal gravity waves, Part I. *J. Atmos. Sci.*, **30**, 1007–1016.

——, 1976a: A simple boundary condition for unbounded hyperbolic flows. *J. Comput. Phys.*, **21**, 251–269.

——, 1976b: The trapeze instability in an equatorial β-plane. *J. Atmos. Sci.*, **33**, 745–763.

——, and L. J. Polinsky, 1977: Spectral distribution of cloud cover over Africa. *J. Meteor. Soc. Japan*, **55**, 483–494.

Shuman, F. G., 1957: Numerical methods in weather prediction: II. Smoothing and filtering. *Mon. Wea. Rev.*, **85**, 357–361.

Sun, W. Y., and I. Orlanski, 1981: Large mesoscale convection and sea breeze circulation. Part II: Nonlinear numerical model. *J. Atmos. Sci.*, **38**, 1694–1706.